JOURNAL OF PROPULSION AND POWER
Vol. 34, No. 3, May–June 2018

Comparative Study of Elliptic and Round Scramjet Combustors Fueled by RP-3

Wei Yao,* Yueming Yuan,† Xiaopeng Li,‡ Jing Wang,§ Kun Wu,¶ and Xuejun Fan**
Key Laboratory of High Temperature Gas Dynamics, Institute of Mechanics, Chinese Academy of Sciences, 100190 Beijing, People's Republic of China

DOI: 10.2514/1.B36721

To explore the combustion performance of nonrectangular supersonic combustors, the flow and combustion characteristics in the round and round-to-elliptic shape-transition scramjet combustors were compared, based on the measurements and the improved delayed detached-eddy simulation modelings. The global equivalence ratio was kept at 0.8, whereas two inlet Mach numbers of 2.5 and 3.0 were tested. To reduce the computational cost, four versions of skeletal mechanisms (respectively, 48 s/197 r, 39 s/153 r, 28 s/92 r, and 19 s/54 r) have been developed for China RP-3 kerosene; and the latest one was used. The predicted static pressure profiles along the streamwise direction were first validated against the measurements. Then, the aerodynamic fields were analyzed for the two combustors to compare their flow, mixing, and combustion performances. The three-dimensional wave structures inside the nonaxisymmetric elliptic combustor were revealed for the first time to show the influence of shape transition. Specifically, the time evolution of the flame structures was analyzed, and dominant modes were extracted by the aid of proper orthogonal decomposition.

Nomenclature

A	=	cross-section area
$a_i(t)$	=	proper orthogonal decomposition mode coefficient
C_{mix}	=	model constant
$c_\alpha \alpha c_k$	=	model constant
c_α	=	molar concentration of species α, mol/m^3
D	=	diameter or ellipse axes, m
$D_\alpha \alpha m^2 D_T$	=	thermal diffusivity, m^2/s
d_{DDES}	=	length scale in delayed detached-eddy simulation, m
D_α	=	mass diffusivity of species α, m^2/s
H	=	absolute enthalpy, J/kg
H_{Ma}	=	height of Mach disk, m
H_t	=	total absolute enthalpy, J/kg
J	=	jet-to-crossflow momentum flux ratio
$k_{f,\beta}$, $k_{r,\beta}$	=	forward and reverse rate constants of the βth-elementary reaction
k_t	=	turbulence kinetic energy, m^2/s^2
L	=	species number
$l_0 l_k$	=	dissipative scale, m
l_0	=	length scale of the mean flow, m
M	=	reaction number
Ma	=	Mach number
$\dot{m}_{\text{fuel,mixed}}$	=	mass flow rates of the mixed fuel, kg/s
$\dot{m}_{\text{fuel,total}}$	=	mass flow rates of the total fuel, kg/s
N	=	mesh cell number
Pr/Pr_t	=	laminar or turbulent Prandtl number
p/P_t	=	static or total pressure, Pa
$Pr/Pr_t\ Q_{\text{air}}/Q_{\text{fuel}}$	=	flow rate of the air crossflow or the fuel jet, g/s
q_i	=	heat flux in the ith direction, W/m^2
R	=	gas constant, J/(kg · K)
Re	=	Reynolds number
R_u	=	universal gas constant; ≈8.314J/(mol · K)
S_{ij}	=	strain rate tensor, m/s
Sc_t	=	turbulent Schmidt number
T/T_t	=	static or total temperature, K
$T_{\text{POD},i}$	=	proper orthogonal decomposition mode of the temperature field, K
t	=	transient physical time, s
u_i	=	velocity in the x_i direction, m/s
u_i'	=	velocity fluctuation in the x_i direction, m/s
W	=	molecular weight, g/mol
x_i	=	Cartesian coordinate in direction i
Y	=	mass fraction
$Y_{f,\text{react}}$	=	fuel mass fraction that can be reacted
y^*	=	nondimensional wall distance
γ_α	=	third-body coefficient for species α
ϵ	=	small quantity to avoid zero division; usually 1×10^{-30}
ϵ	=	turbulence dissipation rate, m^2/s^3
η_c	=	combustion efficiency
η_{mix}	=	mixing efficiency
$\eta_c \eta_t$	=	total pressure loss
λ_i	=	eigenvalue of the autocovariance of the snapshot matrix
ν	=	kinematic viscosity, m^2/s
ν_{eff}	=	effective kinematic viscosity, m^2/s
ν_t	=	turbulent viscosity, m^2/s
$\nu_{\text{eff}}\nu''_{\alpha,k}$, $\nu'_{\alpha,k}$	=	forward and reverse stoichiometric coefficients of the kth reaction
ρ	=	density, kg/m^3
τ_c	=	chemical timescale, s
$\tilde{\tau}_{ij}\tau_{ij}$	=	Reynolds stress tensor, kg/(m · s^2)
$\tau_c \tau_k$	=	Kolmogorov timescale, s
τ_{mix}	=	micromixing timescale, s
$\tilde{\tau}_{ij}$	=	viscous stress tensor, kg/(m · s^2)
$\omega_\alpha \alpha \Phi$	=	global equivalence ratio
$\Psi_{T,j}$	=	turbulent enthalpy flux, W/m^2

Presented as Paper 2017-2190 at the 21st AIAA International Space Planes and Hypersonics Technologies Conference, Xiamen, P.R. China, 6–9 March 2017; received 10 April 2017; revision received 29 September 2017; accepted for publication 29 September 2017; published online Open Access 16 November 2017.

*Associate Professor; also School of Engineering Science, University of the Chinese Academy of Sciences, 100049 Beijing, People's Republic of China; weiyao@imech.ac.cn. Member AIAA.
†Assistant Professor; yuanym@imech.ac.cn. Member AIAA.
‡Postdoctor; also Chinese Academy of Sciences; lixiaopeng@iet.cn.
§Senior Engineer; also Chinese Academy of Sciences; wangjing@imech.ac.cn.
¶Ph.D. Student; also Chinese Academy of Sciences; wukun@imech.ac.cn.
**Professor; also Chinese Academy of Sciences, School of Engineering Science, University of the Chinese Academy of Sciences, 100049 Beijing, PRC; xfan@imech.ac.cn. Lifetime Member AIAA (Corresponding Author).

$\Psi_{\alpha,j}$ = turbulent species diffusion flux, kg/(m^2 · s)
ω_α = mass production of species α, kg/(m^3 · s)

Subscripts

air = quantity of the air crossflow
CO_2 = carbon dioxide
f = fuel quantity
i, j = direction indices
Inlet = quantity on the inlet plane
st = quantity at stoichiometric condition
x = location in the streamwise direction
α = species index
β = reaction index

Superscripts

~ = Favre-averaged quantity
– = averaged quantity

I. Introduction

TRADITIONAL scramjet combustors are usually designed to be rectangular in the cross section to enable a tight integration of the hypersonic inlet with the planar vehicle body, which is desirable because the flow angle approaching the inlet will then be less affected by the vehicle angle of attack. Although nonrectangular combustors, such as those with axisymmetric and elliptic burner cross sections, also have unique advantages and are receiving increasing research interest. Compared with traditional rectangular combustors, nonrectangular combustors can avoid the influence of corners on the development of boundary-layer and wave structures, improve the contact area between the transverse fuel jet(s) and the air crossflow, and contribute to the structural strength and weight reduction of the combustor. To gain both the advantages of the rectangular inlet and nonrectangular combustor, a practical approach is to combine them with a smooth transition part. One example is the concept of rectangular-to-elliptic shape transition, which was proposed in [1–4]. To date, most of the reported supersonic combustor studies have been for rectangular scramjet combustors; whereas the flow, mixing, and combustion characteristics in nonrectangular combustors have been poorly understood and still not enough research efforts have been dedicated to this area. Possibly the earliest experimental tests on round and elliptic supersonic combustors were reported in the 1960s [5]; however, an in-depth analysis on the aerodynamic and combustion characteristics was an unattainable goal without the help of computational fluid dynamics modeling at that time. Then, with the advance of experimental and computational techniques, optical visualization of the internal flowpath and high-fidelity modelings became available. In recent years, the experimental and modeling studies of round [6–9] and elliptic [1–4] scramjet combustors regained new attention by independent research entities.

The change in the cross-section shape of the flowpath influences not only the injection depth but also the development of the viscous boundary layer. In the elliptic combustor, the reduced depth in the minor axis direction is favorable for the mixing between the transverse jet and the crossflow. The shape transition from the round inlet/isolator to the following elliptic burner section will cause a nonequilibrium turbulent boundary layer because the shape factor (the ratio of displacement thickness to momentum thickness) has been changed by the local curvature [10]. Then, the resistance of the boundary layer to the thickening and separation changes. Accordingly, the wave structures in the upstream deform to affect the downstream fuel injection, mixing, and combustion. The elliptic section will especially produce nonaxisymmetric wave structures as well as complex shock-wave/turbulent boundary-layer interactions, which have been reported in [1,2]; but, their three-dimensional structures have never been revealed. In addition, the nonuniform wall heat flux distribution due to uneven fuel injections around the elliptic combustors will give rise to great difficulty in the layout of cooling channels. Therefore, the dominant flame patterns in the elliptic combustor should be analyzed to forecast any local overheating. In summary, a close observation of the effect of asymmetry on the internal flow and combustion should be made first to facilitate the design of combustors with shape transition.

In this study, two typical nonrectangular combustors in elliptic and round cross sections, respectively, are modeled and validated against the experimental tests. For each combustor, two cases at different crossflow Mach numbers Ma of 2.5 and 3.0 are studied, whereas the global equivalence ratio is kept the same. The crossflows at a raised enthalpy both correspond to a flight Mach number Ma of 6.5. Supercritical China RP-3 kerosene is transversely injected at supersonic speed through a group of flush-wall circular injectors circumferentially distributed upstream of the cavity. First, the static pressure along the streamwise direction is compared with the measurement to validate the modeling results. Then, the flow, mixing, and combustion characteristics are compared and analyzed for the elliptic and round combustors. The three-dimensional wave structures inside the elliptic combustor are first shown to reveal the influence of nonaxisymmetric cross-section on the shock train and the Mach number Ma field. The time evolution of the flame structures is especially analyzed, and dominant flame modes are extracted by the aid of proper orthogonal decomposition (POD).

II. Numerical models

A. Governing Equations

The unsteady and three-dimensional Favre-averaged compressible Navier–Stokes equations are solved for multicomponent reactive gas mixtures, which are represented by a set of conservative variables ($\bar{\rho}$, $\tilde{u}_j$, $\tilde{H}_t$, $\tilde{Y}_\alpha$):

$$\frac{\partial \bar{\rho}}{\partial t} + \frac{\partial \bar{\rho}\tilde{u}_j}{\partial x_j} = 0 \tag{1}$$

$$\frac{\partial \bar{\rho}\tilde{u}_i}{\partial t} + \frac{\partial \bar{\rho}\tilde{u}_j\tilde{u}_i}{\partial x_j} + \frac{\partial \bar{p}}{\partial x_j} - \frac{\partial \tilde{\tau}_{ij}}{\partial x_j} = -\frac{\partial \tau_{ij}}{\partial x_j} \tag{2}$$

$$\frac{\partial \bar{\rho}\tilde{H}_t}{\partial t} + \frac{\partial \bar{\rho}\tilde{u}_j\tilde{H}_t}{\partial x_j} - \frac{\partial}{\partial x_j}\left(\bar{\rho}D_T\frac{\partial \tilde{H}_t}{\partial x_j}\right) - \frac{\partial \bar{p}}{\partial t} - \frac{\partial \tilde{u}_j\tilde{\tau}_{ij}}{\partial x_j} = -\frac{\partial \Psi_{T,j}}{\partial x_j} \tag{3}$$

$$\frac{\partial \bar{\rho}\tilde{Y}_\alpha}{\partial t} + \frac{\partial \bar{\rho}\tilde{u}_j\tilde{Y}_\alpha}{\partial x_j} - \frac{\partial}{\partial x_j}\left(\bar{\rho}D_\alpha\frac{\partial \tilde{Y}_\alpha}{\partial x_j}\right) = -\frac{\partial \Psi_{\alpha,j}}{\partial x_j} + \bar{\omega}_\alpha \tag{4}$$

$$\bar{p} = \bar{\rho}R\tilde{T} \tag{5}$$

Here, the bar (-) and the tilde (~) represent averaged or Favre-averaged quantities, respectively; t denotes the time; x_i is the Cartesian coordinate in direction i; $\bar{\rho}$ is the density; $\tilde{u}_j$ is the velocity component in the x_i direction (spatial dimension of $i = 1, 2, 3$); $\bar{p}$ is the pressure; $\tilde{\tau}_{ij}$ is the viscous stress tensor; $\tilde{H}_t = \tilde{H} + 0.5\tilde{u}_i^2$ is the total absolute enthalpy defined as the sum of the absolute enthalpy $\tilde{H}$; the resolved kinetic energy q_i is the heat flux vector in the ith direction; $\tilde{Y}_\alpha$ is the mass fraction of species α ($\alpha = 1, \ldots, N$, where N is the total species number); $\bar{\omega}_\alpha$ is the averaged mass production rate of chemical species α; D_α is the mixture-averaged mass diffusivity of species α; D_T is the thermal diffusivity; and $\tilde{T}$ is the temperature. The real-gas effect is only accounted for in the very small amount of fuel in the injection tube(s), whereas the density of the rest of the gas is calculated based on the ideal gas law. For the ideal gas, $R = R_u/W$ is the gas constant, $R_u = 8.314$ J · mol^{-1} · K^{-1} is the universal gas constant, and

$$W = \left(\sum_{k=1}^{N} Y_\alpha/W_\alpha\right)^{-1}$$

is the molar weight of the multicomponent mixture. For the real gas, R is calculated based on the principle of extended corresponding states (ECSs). The Soret and Dufour effects are neglected in the current modelings. The computable average momentum diffusive flux is given by

$$\tilde{\tau}_{ij} = \bar{\rho}\nu(\tilde{T})\left(2\tilde{S}_{ij} - \frac{2}{3}\delta_{ij}\tilde{S}_{kk}\right) \tag{6}$$

where the kinetic viscosity ν is a function of $\tilde{T}$, and the computable strain-rate tensor of the resolved scales is formulated as

$$\tilde{S}_{ij} = \frac{1}{2}\left(\frac{\partial \tilde{u}_i}{\partial x_j} + \frac{\partial \tilde{u}_j}{\partial x_i}\right) \tag{7}$$

The Reynolds stresses τ_{ij} and turbulent fluxes ($H_{t,ij}$ and $\Phi_{\alpha,j}$) in Eqs. (1–5) are unclosed and require specific modeling. The Reynolds stress, defined as $\tau_{ij} = \bar{\rho}(\widetilde{u_i u_j} - \tilde{u}_i\tilde{u}_j)$, is modeled by the Boussinesq hypothesis, where the Reynolds stresses are taken to be proportional to the local strain rate of the resolved flow:

$$\tau_{ij} = -2\bar{\rho}\nu_t\tilde{S}_{ij} + \frac{2}{3}\delta_{ij}\bar{\rho}k_t \tag{8}$$

Here, ν_t is the turbulent viscosity given by an approximate turbulence model, and k_t is the unresolved turbulence kinetic energy.

The turbulent enthalpy flux $\Psi_{T,j} = \bar{\rho}(\widetilde{u_j H_t} - \tilde{u}_j\tilde{H}_t)$ is modeled by a gradient diffusion assumption as

$$\Psi_{T,j} = -2\bar{\rho}\frac{\nu_t}{Pr_t}\frac{\partial \tilde{H}_t}{\partial x_j} \tag{9}$$

where Pr_t is the turbulent Prandtl number.

The turbulent species diffusion flux $\Psi_{\alpha,j} = \bar{\rho}(\widetilde{u_j Y_\alpha} - \tilde{u}_j\tilde{Y}_\alpha)$ is also modeled using the gradient diffusion assumption as

$$\Psi_{\alpha,j} = -2\bar{\rho}\frac{\nu_t}{Sc_t}\frac{\partial \tilde{Y}_\alpha}{\partial x_j} \tag{10}$$

where Sc_t is the turbulent Schmidt number.

The preceding Favre-averaged equations provide a uniform framework for the modeling in Reynolds-averaged Navier–Stokes (RANS) or large-eddy simulations (LESs), differentiating in that the average operation is the Reynolds average in the RANS mode and the spatial filter in the LES mode. The Reynolds stresses and turbulent fluxes are slightly different in the two modes: for example, $\tau_{ij} = -\bar{\rho}\,\widetilde{u_i' u_j'}$ for RANS, but the subgrid-scale (SGS) stresses in the LES are contributed by the Leonard stresses, the cross stresses and the LES stresses because the turbulent fluctuations can be partially resolved by the fine LES mesh. However, in the current versions of finite volume method, the different terms in the SGS stresses are lumped together and modeled in whole as a single entity by using the same Boussinesq hypothesis. Both the turbulent viscosity in the RANS mode and the SGS viscosity in the LES mode simulate the influence of unresolved eddies to the resolved scales, which form the basis of hybrid RANS/LES approaches. The numerical treatments in resolving Eqs. (1–10) are the same for any turbulence models, and the switch between RANS or LES is determined by which turbulence model the eddy viscosity is calculated.

The thermodynamic and transport properties of the gas mixture (such as the absolute enthalpy, the specific heat, the viscosity, and the thermal and mass diffusivities) are calculated using the chemical kinetics package CHEMKIN-II [11] based on the Joint U.S. Army/Navy/NASA/Air Force (known as JANAF) thermochemical table [12] and a CHEMKIN-format transport database. The viscosity, specific heat, and conductivity are all independent of pressure but only depend on temperature. The mixture-averaged viscosity and thermal conductivity are calculated using the modified Wilkes law [13] and combination averaging [14], respectively. Mixture-averaged mass diffusivities are used, and the mass conservation is achieved by setting the nitrogen as inert gas, for which the mass fraction is computed simply by subtracting the sum of the remaining mass fractions from unity. The thermal diffusivity is estimated as ν/Pr with a unity laminar Prandtl number ($Pr = 1.0$).

B. Turbulence Model

To properly resolve the turbulent boundary layer and alleviate the huge computation cost, it is required that the RANS mode fully cover the boundary layer. In the original detached-eddy simulation (known as DES97) technique [15], the transition from RANS to LES was solely determined by the mesh resolution. Thus, DES97 has strict requirements on the near-wall meshing, i.e., the nondimensional normal wall distance $y^* \sim o(1)$ and the wall-parallel grid spacing exceeding the thickness of the boundary layer. However, the thickness of the boundary layer and the viscosity-affected sublayer is usually unknown before the modelings. Thus, the near-wall meshing may not guarantee the aforementioned requirements. To avoid the aforementioned requirements on wall-normal and -parallel grid spacing, the improved delayed detached-eddy simulation (IDDES) [16] is employed in this study to enable an automatic determination of the local boundary-layer thickness and weaken the influence of near-wall meshing on the internal flowfields.

The spatial-filtered or Reynolds-averaged equations are solved in a uniform framework by equivalently treating the turbulent viscosity in the RANS mode and the subgrid-scale viscosity in the LES mode. The background RANS model in the IDDES approach is the one-equation Spalart–Allmaras model [17]. Gradient diffusion models with constant turbulent Prandtl Pr_t and Schmidt Sc_t numbers of 1.0 are used to account for the heat and mass diffusion due to unresolved turbulent eddies.

C. Kerosene Mechanism Reduction and Turbulent Combustion Modeling

The detailed kerosene mechanism (2815 s/8217 r) proposed by Dagaut et al. [18] was reduced under the typical working conditions of scramjet combustors: i.e., equivalence ratio of 0.6–1.4, static pressure of 0.5–3.0 bar, and static temperature of 300–3000 K. Four versions of skeletal mechanisms [respectively, 48 s/197 r [19], 39 s/153 r [20], 28s/92r [21], and 19 s/54 r (Table A1)] have been developed for China RP-3 kerosene by using the directed relation graph with error propagation and sensitivity analysis method [22] together with the manual path analysis.

Although the mechanism size has been significantly reduced, the key kinetic properties (such as adiabatic flame temperature, total heat release, ignition delay, and laminar flame speed) agree well with the original detailed mechanism, as shown in Fig. 1. The adiabatic flame temperature, total heat release, and ignition delay shown in Figs 1a–1c were calculated in a closed homogeneous adiabatic reactor under a constant pressure of 1 atm and an initial volume of 1 cm^3. The initial mixture temperature varied from 1200 to 2400 K for each parameter study case. The starting gas mixture was a stoichiometric mixture of kerosene (28.8% isooctane, 62.4% n-decane, and 8.8% n-propylcyclohexane in mass fraction) and air [21% oxygen (O_2) and 79% nitrogen (N_2)]. The laminar flame speed in Fig. 1d was calculated for an adiabatic, atmospheric pressure, and stoichiometric kerosene/air mixture at an initial temperature of 473 K and equivalence ratios from 0.7 to 1.5. In this study, the latest version of the reduced RP-3 kerosene mechanisms (i.e., the listed one in Table A1 with 19 s/54 r) will be used.

In this study, the turbulence–chemistry interaction is accounted for by the partially stirred reactor (PaSR) model [23]. The final averaged reaction rate $\bar{\omega}_\alpha$ in the PaSR is mutually determined by the characteristic timescales of chemical reactions τ_c and turbulent micromixing τ_{mix}:

$$\bar{\omega}_\alpha = \frac{\tau_c}{\tau_c + \tau_{\mathrm{mix}}}\omega_\alpha \tag{11}$$

where ω_α is the reaction rate over the current integration time step calculated from the Arrhenius law:

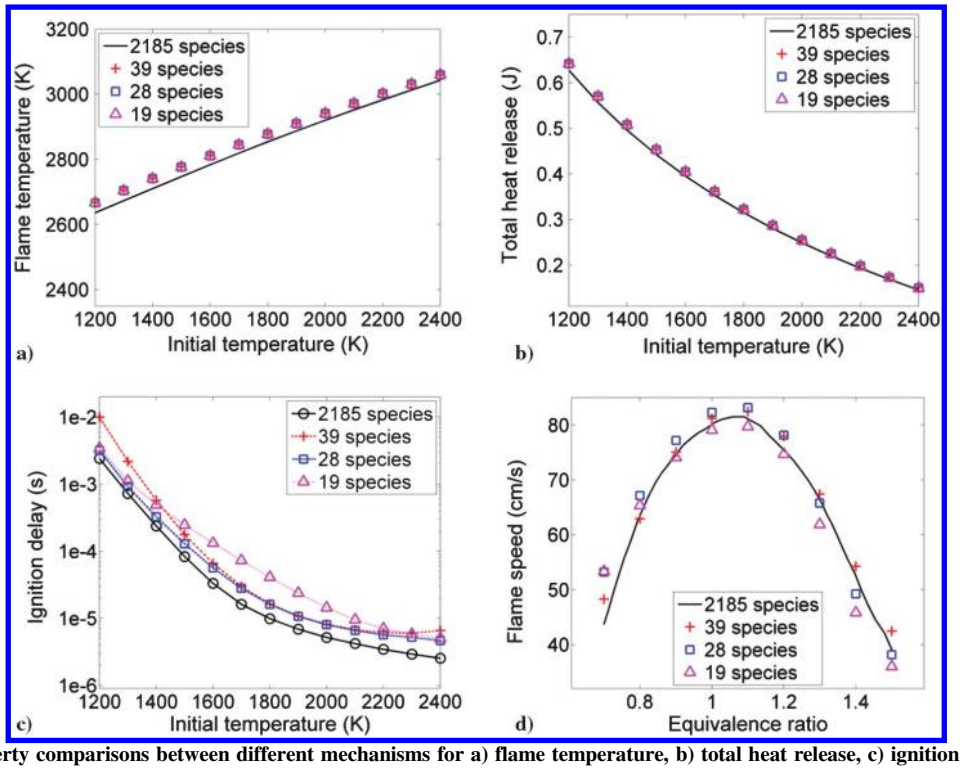

Fig. 1 Kinetic property comparisons between different mechanisms for a) flame temperature, b) total heat release, c) ignition delay in logarithmic ordinate, and d) laminar flame speed.

$$\omega_\alpha = \sum_{\beta=1}^{M} \omega_{\alpha,\beta} = \sum_{\beta=1}^{M} W_\alpha(\nu''_{\alpha,\beta} - \nu'_{\alpha,\beta})\left(k_{f,\beta}\prod_{\alpha=1}^{L}[c_\alpha]^{\nu'_{\alpha,\beta}} - k_{r,\beta}\prod_{\alpha=1}^{L}[c_\alpha]^{\nu''_{\alpha,\beta}}\right) \quad (12)$$

where $\nu''_{\alpha,\beta}$ and $k_{f,\beta}$, respectively, indicate the forward stoichiometric coefficient and the forward rate constant of the βth-elementary reaction, whereas $\nu'_{\alpha,\beta}$ and $k_{r,\beta}$ are their reverse counterparts; and L and M are, respectively, the total numbers of species and elementary reactions. The rate constants follow the Arrhenius law, with the Arrhenius coefficients given in Table A1; and c_α is the molar concentration of species α. An in situ adaptive tabulation table [24] is constructed locally to each processor to speed up the solving of stiff chemistry systems. The micromixing timescale τ_{mix} is defined as $\tau_{\text{mix}} = C_{\text{mix}}(\nu_{\text{eff}}/\epsilon)^{1/2}$ with $C_{\text{mix}} = 1.0$ [25]. The dissipation rate ϵ is estimated as $\epsilon = 2\nu_{\text{eff}}|\tilde{S}_{ij}|^2$, with $\nu_{\text{eff}} = \nu_t + \nu$ and $c_k = 0.07$. Usually, the characteristic chemical timescale τ_c is calculated as the reciprocal of the elements of the Jacobian matrix $(\partial(\omega_\alpha/W_\alpha)/\partial c_\alpha)^{-1}$, for which the results of τ_c are essentially the same with $c_\alpha/(\omega_\alpha/W_\alpha)$. Different elementary reactions can have extremely different chemical timescales varying by orders of magnitude, causing a stiff problem in solving the chemistry and, on the other side, making difficulty in determining an approximate overall chemical timescale for multicomponent mixtures. In this study, the overall chemical timescale is estimated as the ratio of the summation of species concentrations to that of forward production rates:

$$\tau_c = \sum c_\alpha / \max\left(\sum(\omega_\alpha^+/W_\alpha), \varepsilon\right)$$

with ε as a small quantity. Here, the forward production rates are calculated by only considering the forward reactions and neglecting all their reverse counterparts.

D. Test Facility and Case Setup

Both the round and elliptic combustors are tested in a continuous-flow supersonic combustion test facility. The test facility can simulate flight Mach numbers Ma of four to seven and altitudes of 16–28 km. The vitiated air heater provides high-enthalpy incoming flow with total temperatures of 900–2000 K and flow rates of 2.5–5.0 kg/s through burning hydrogen with oxygen replenishment in the airstream. Liquid China RP-3 kerosene heated to supercritical status by an electric ceramic heater is delivered to the test article as the fuel.

Figure 2a shows the schematics of the round and the round-to-elliptic shape-transition (RdEST) scramjet combustors. The scramjet combustors are composed of three sections: a 600-mm-long isolator section with a 0.7 deg divergence angle, an 800-mm-long burner section, and a 600-mm-long expander section with a 4 deg divergence angle. The inlet diameters of the isolator, burner, and expander sections are 125, 132, and 170 mm, respectively. The diameter of the expander outlet is 212 mm. The burner section is changeable between the elliptic and round modules. The elliptic burner section was designed to have the same cross-section area, with the round one at the same streamwise location. Figure 2b shows the schematic of the elliptic burner section. In the elliptic burner section, the shortest semiminor axis is 50 mm and the longest semimajor axis is 115.5 mm, which are both located on a cross section 425 mm downstream of the burner inlet and between the upstream and downstream cavities. There are two circumvented cavities assembled in tandem in the burner section for flame anchoring and possible reignition. The upstream and downstream cavities are at the same streamwise locations for the elliptic and the round burners, i.e., 228 and 578 mm from the burner inlet, respectively, to the leading edges of the cavities. Both the cavities have a depth of 15 mm and a length–depth ratio of seven, and thus are classified as open cavities. The aft walls of the cavities are at an angle of 45 deg relative to the cavity floor. The fuel (supercritical RP-3 kerosene) is injected at 56 mm upstream of the upstream cavity for both burner sections. Portholes are reserved at the same distance before the downstream cavity for the future tailored injection study. For the round section, the supercritical RP-3 kerosene is injected from eight 2-mm-diam evenly spaced, circular injectors. For the elliptic section, the number of injection portholes is reduced to six, with no injection on the plane through the

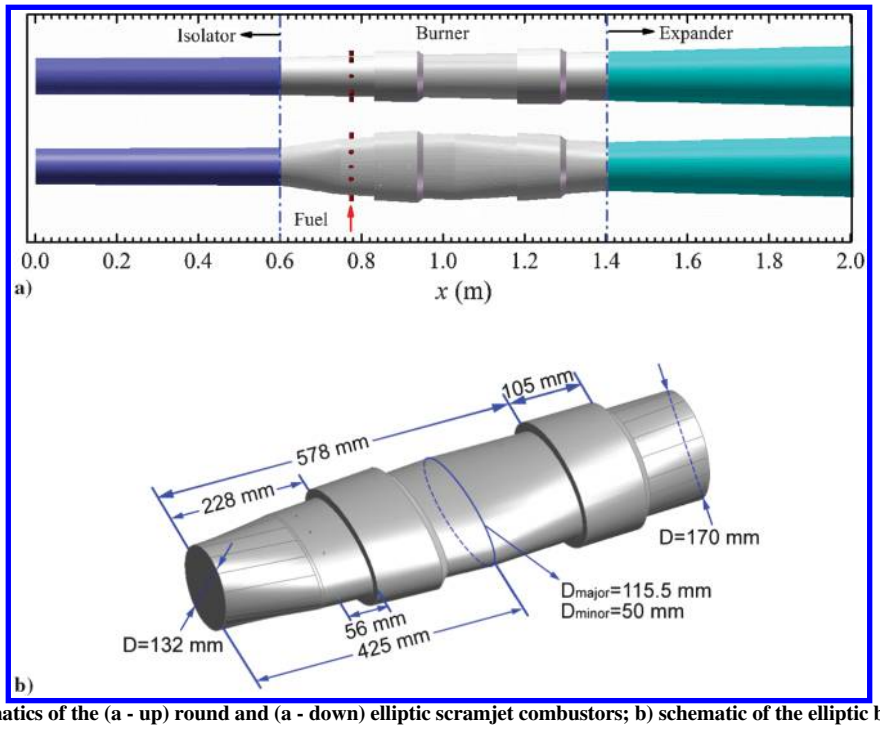

Fig. 2 Schematics of the (a - up) round and (a - down) elliptic scramjet combustors; b) schematic of the elliptic burner section.

major axis. The diameter of fuel portholes is enlarged to 2.5 mm for the elliptic section to accommodate the reduction in number. Static pressure is measured by Motorola MPX2200 pressure transducers along the inner wall with 50 mm intervals.

The four tests are summarized in Table 1, with the incoming air crossflows all corresponding to a flight Mach number Ma of 6.5. The incoming vitiated air, which is supplied by burning hydrogen in the air with oxygen replenishment, has a raised stagnation temperature of 1600 K and a mass flow rate of 3.6 kg/s at the isolator inlet. The compositions of vitiated air are N_2 in 60.5% mole fraction, O_2 in 21.7%, and H_2O in 17.8%. The global equivalence ratio is kept at $\Phi = 0.8$ for all the cases, whereas the inlet Mach number Ma changes from 2.5 to 3.0. The China RP-3 kerosene is preheated to above its critical temperature of 630 K to reduce the gasification time and enhance the mixing. The combustor walls are exposed directly to the hot combustion gas without any active-cooling facility. However, no significant melting damage to the wall surface was observed after the 27 s test, indicating that the wall temperature was still within the thermal limit (~1300 K) of the wall material. The time sequences of the test procedures (e.g., vitiated air heating and injection, fuel injection, hydrogen ignition, and final flush washing) and data acquisition were automatically controlled.

E. AstroFoam Developed from OpenFOAM and Other Numerical Details

The modeling is performed by the compressible reacting flow solver AstroFoam, which was developed on the basis of the compressible flow solver rhoCentralFoam distributed with OpenFOAM Version 3.0.1 [26] mainly through adding the features of multispecies transport and multicomponent reaction. AstroFoam, together with the original rhoCentralFoam solver, was first validated for various frozen flows, including the canonical shock tube problem, forward step flow, hypersonic flow over a biconic, and supersonic jets [26–29]. The solver was then applied for various scramjet combustor cases [20,21] to examine its accuracy and robustness in the engineering modeling of supersonic combustion.

The computational domain contains the isolator, burner, and expander sections in their full size. Due to the bilateral symmetry of the combustors, a one-eighth split domain (in the radial direction) for the round combustor and a quarterly split domain for the elliptic combustor are modeled with symmetrical boundary condition applied to the splitting planes. Such an asymmetric boundary treatment has been widely used in the LES modeling of symmetric or axisymmetric scramjet combustors [8,9,30,31], mainly to alleviate the huge computational cost. The unstructured mesh is generated using the Cartesian cut-cell method, which uses a patch-independent volume meshing approach with the surface mesh automatically created from the boundary of volume mesh. The Cartesian cut-cell method can produce high-quality uniform hexahedral grid cells for the most internal volume of the computational domain, whereas tetrahedron, wedge, or pyramid cells are filled only in large-curvature regions, e.g., near the borders or corners. The whole domain is meshed first with uniform 1 mm cells, which are then adaptively refined based on the local curvature and the size function. An inflation layer consisting of 23 prism layers is laid on the wall boundaries. The initial prism layer height closest to the wall is 5 μm, which corresponds to a nondimensional cell size of $y^* < 1$ on all the wall surfaces for the examined combustor flows. The inflation layer has an average thickness of 2 mm, with the last prism located in the logarithmic layer. In addition to the inflation layer, the mesh in and around the jet porthole is progressively refined to 1/16th of the cell size in the main domain, as shown in Fig. 3. The current minimum cell

Table 1 Summary of test configurations

Vitiated air crossflow				RP-3 jet				Injector	Combustor
$P_{t,\text{air}}$ MPa	$T_{t,\text{air}}$ K	Q_{air} g/s	Ma	$P_{t,f}$ MPa	$T_{t,f}$ K	Q_{fuel} g/s	ϕ	Numbers	Burner shape
0.85	1615.5	3575.9	2.5	5.52	789	212.8	0.8	6	elliptic
0.85	1611.2	3602.7		3.77	788	212.6	0.8	8	round
13.66	1581.7	3578.9	3.0	5.77	784	218.1	0.8	6	elliptic
13.66	1661.1	3557.1		5.74	792	214.9	0.8	8	round

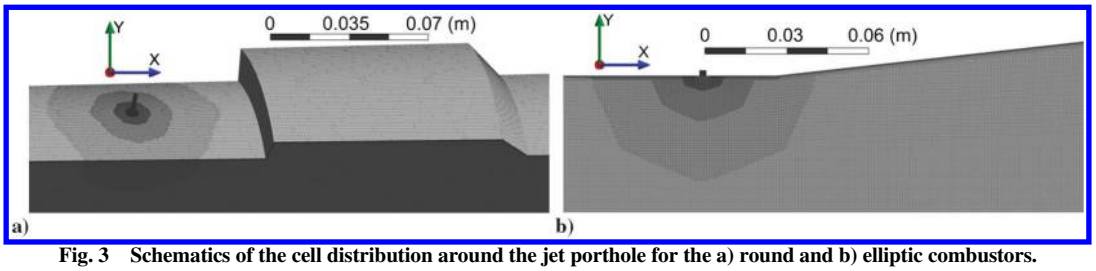

Fig. 3 Schematics of the cell distribution around the jet porthole for the a) round and b) elliptic combustors.

size of 62.5 μm is comparable to the Kolmogorov scale of 50 μm. The total cell number in the split combustor domain is 10.65 million for the round combustor and 27.43 million for the elliptic combustor. For the elliptic combustor, 99.3% of the volume is meshed by hexahedral cells, 96.85% of the volume has a skewness smaller than 0.1, and 97.13% of the volume has an orthogonal quality higher than 0.98. For the round combustor, 98.2% of the volume is meshed by hexahedral cells, 96.02% of the volume has a skewness smaller than 0.25, and 97.63% of the volume has an orthogonal quality higher than 0.9. The grid quality for the round combustor is still good, but it is not as excellent as that of the elliptic one because plenty of prism layers are generated to envelop the wedge geometry. The wide existence of hexahedral cells and high cell orthogonality suggest that the mesh sets have high interpolation accuracy and excellent numerical stability. In the following analysis, the coordinate origin is located at the center of the inlet plane of the isolator section viewed from outside, with x denoting the streamwise direction.

The fixed pressure, temperature, and velocity on the isolator inlet and the fuel inlets are set according to those listed in Table 1. For China RP-3 kerosene, the ECS is used to calculate the fuel injection velocity from the mass flow rate because the compressibility of supercritical RP-3 kerosene cannot be described by the ideal gas law. The real gas effect accounted for by the ECS is only included for the fuel in the tube ($c_{\text{fuel}} \geq 80\%$). Once the fuel has been injected into the crossflow, it will be quickly diluted; and then the mixture is considered to obey the ideal gas law. A RANS-type turbulent inlet boundary condition is specified on the isolator inlet by fixing a turbulence viscosity corresponding to $\nu_t/\nu = 1$. The open boundary condition is applied to the expander outlet, where a zero gradient is used for outflow and ambient flow conditions for the temperature and gas composition are specified should backflow occur. The inner wall temperature along the streamwise direction is specified as a linear function varying from 500 K at the isolator inlet to 1200 K at the expander outlet.

The computations are performed in parallel at the National Supercomputing Center of Tianjin (TH-1) using 240 CPU cores. The time step is limited by both a maximum Courant number of 0.3 and a user-specified maximum time step of 5×10^{-8} s to avoid the spurious undulating flowfields caused by excessive convection. The maximum time restriction is chosen to be roughly 1/10th ~1/20th of the chemical timescale to make the species variation in one time step not cause large errors in estimating the flow properties. Each modeling case costs about 150,000 CPU hours to ensure three flushthrough times (FTTs) of ≈4 ms over the whole combustor flowpath for data sampling and statistics before another three FTTs to reach the quasi-steady flow status.

III. Results and Discussion

A. Comparison of Aerodynamic Fields

First, a grid sensitivity analysis is conducted for the elliptic case operated at Ma = 3.0. The mesh with 27.43 million cells and a maximum cell size of 1 mm is used as the comparison base. Then, the mesh in the whole domain is refined to reach 36.25 million cells with a maximum cell size of 0.8 mm and 46.17 million cells with a maximum cell size of 0.65 mm, respectively. A coarser mesh of 17.16 million cells with a maximum cell size of 1.2 mm is also made for comparison. From the comparison in Fig. 4a, the prediction discrepancies for the mesh sets with 27.43 and more million cells are small and can be considered as almost identical in the whole flowpath, whereas the mesh set with 17.16 million cells underpredicts the overall pressure by a maximum of 10%. For transverse jet flames, the jet penetration may have an important impact on the overall jet mixing and then pressure rise. Thus, the local mesh around the jet portholes is further refined to reach a minimum size of 80 μm and a total cell number of 49.16 million. However, from the comparison, it seems that the pressure profile is insensitive to the refinement. Figure 4b shows the variation of the peak pressure normalized by the one with 27.43 million cells versus the characterize mesh size defined conveniently as $N^{-1/3}$, with N as the cell number. The discrepancy between those predicted by the finest mesh (46.17 million cells) and the base mesh (27.43 million cells) is 4.3%, whereas the coarser mesh (17.16 million cells) produces an error of 8.3%. The locally refined mesh (49.16 million cells) predicts a minor discrepancy of 0.3% as compared with the mesh set with 46.17 million cells. In consideration of the complexity of the modeling of scramjet combustors, the peak discrepancies within 5% and the almost identical overall profiles are satisfactory. Thus, in the following case calculations, the mesh sets configured with a maximum size of 1 mm will be used to alleviate the computational cost in the case studies.

Figure 5 compares the measured and predicted static pressure along the streamwise direction. Three repeated measurements at different times during the quasi-steady period are plotted. The data were collected on the plane through the major axis for the elliptic combustor. The predictions seem to be better for the Ma = 3.0 case, where both the pressure rise ratio and the initial pressure rise location

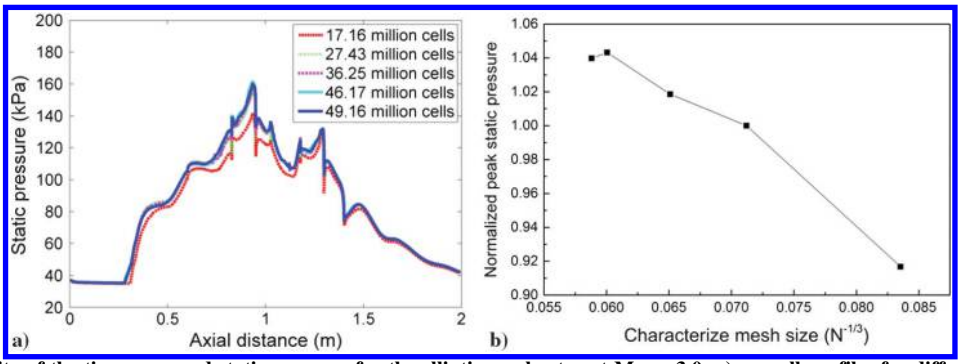

Fig. 4 Grid sensitivity of the time-averaged static pressure for the elliptic combustor at Ma = 3.0: a) overall profiles for different mesh resolutions, b) normalized peak static pressure versus characterize mesh size.

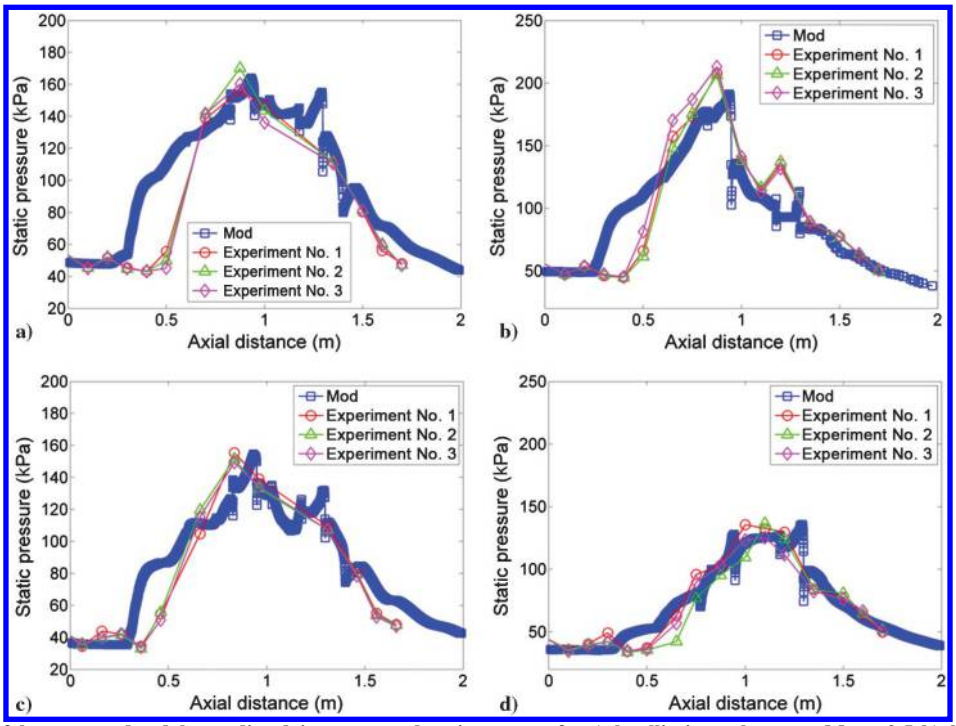

Fig. 5 Comparison of the measured and the predicted time-averaged static pressure for a) the elliptic combustor at Ma = 2.5, b) the round combustor at Ma = 2.5, c) the elliptic combustor at Ma = 3.0, and d) the round combustor at Ma = 3.0.

are well predicted, indicating that the flame anchoring location and the distribution of wave structures inside the combustor are close to the real situation. For the Ma = 2.5 cases, the pressure rise ratios are well predicted, but the predicted initial pressure rise locations, which correspond to the feet of the first oblique shock waves, shift upstream for about 10 cm. The location of the first shock wave is mainly determined by the backpressure and the boundary-layer separation. Because the predicted pressure rise ratio is in accordance with the experimental data, the disagreement can only be attributed to the uncertainty in the boundary-layer modeling. As observed, the shifting distance of the shock train is roughly proportional to the boundary-layer displacement thickness, which increases with the increasing of Mach number Ma and decreases with the increasing Reynolds number *Re*. At a lower inlet Mach number Ma (e.g., 2.5), the Reynolds number *Re* decreases as well (the same flow flux but higher static temperature). Thus, their effects counteract somewhat. Note that some factors may not be taken into account in the current modelings: for example, the wall roughness and the inflow turbulence, which influence the initial pressure rise location through changing the boundary-layer thickness. Further studies are needed to examine the influencing factors for the initial shock train location.

Figures 6–9, respectively, compare the instantaneous fields of the Mach number Ma, fuel mass fraction, static temperature, and numerical shadowgraph for the elliptic and the round combustors operated at different inlet Mach numbers Ma. The two-dimensional contours are extracted on the plane through the injector for the round combustor, as well as through the minor axis for the elliptic combustor. The continuous regions enclosed by the black sonic lines (Ma = 1) in Fig. 6 indicate that all combustors actually run in scramjet mode. The subsonic regions on the shown planes are obviously larger for the round combustors. As the Mach number Ma rises from 2.5 to 3.0, the initial location of the shock train remains almost the same for the elliptic combustor, whereas it considerably slides downstream at a distance of $1D_{\text{inlet}}$ (D_{inlet} is the diameter of the isolator inlet) for the round combustor. Because the downstream mixing and combustion efficiencies are strongly influenced by the sliding of the shock train, the elliptic combustor is supposed to have better combustion stability. The change of the burner section from a round to an elliptic cross section is to increase the mixing of the jet with the air crossflow by using the shorter minor axis. However, from Fig. 6 and the close-up view of the fuel jets in Fig. 7, it is evident that the jet penetration depth decreases for the elliptic combustor cases. The jets tilt heavily toward the wall for the elliptic combustor cases while penetrating straightly and deeply into the crossflow for the round combustor cases. The jet-to-crossflow momentum flux ratio *J* of the round to the elliptic combustor cases is about 1.1 for each jet porthole, according to the relationship $H_{\text{Ma}}/D_f \sim \text{J}^{0.656}$ [32]. The penetration depth denoted by the height of Mach disk H_{Ma} should be

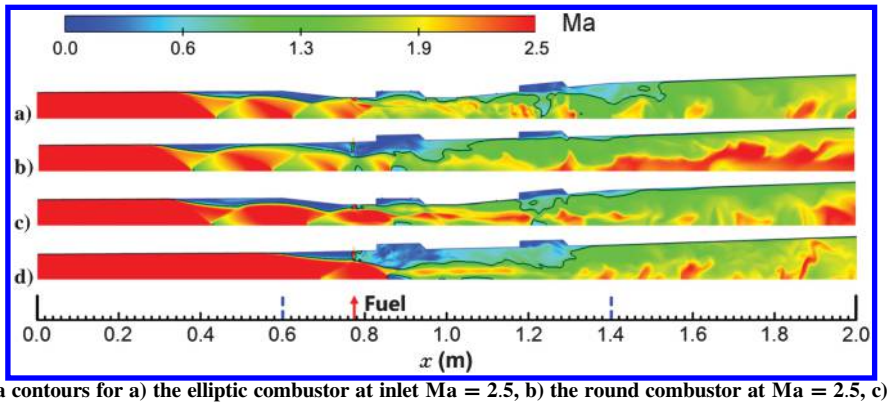

Fig. 6 Instantaneous Ma contours for a) the elliptic combustor at inlet Ma = 2.5, b) the round combustor at Ma = 2.5, c) the elliptic combustor at Ma = 3.0, and d) the round combustor at Ma = 3.0.

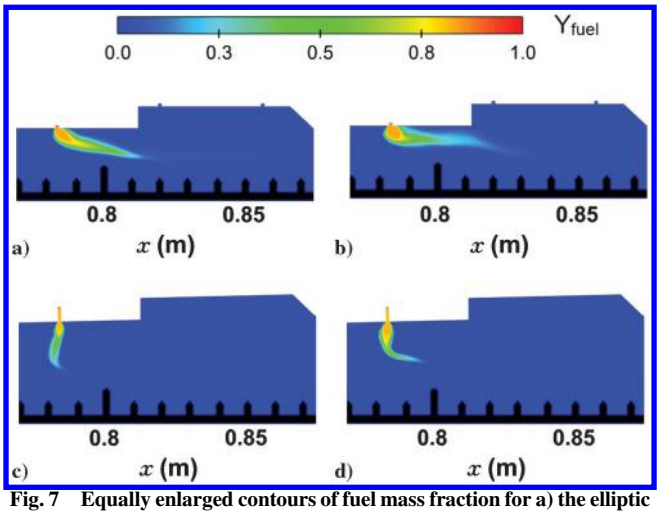

Fig. 7 Equally enlarged contours of fuel mass fraction for a) the elliptic combustor at Ma = 2.5, b) the elliptic combustor at Ma = 3.0, c) the round combustor at Ma = 2.5, and d) the round combustor at Ma = 3.0.

smaller for the round combustor cases because the diameter of the fuel porthole D_f has been increased for the elliptic combustor. However, this is contrary to the observation of an obviously higher jet penetration depth for the round combustor cases. The only explanation is possible that the momentum flux of the local crossflow has been changed significantly by the shape transition in the cross section, as indicated by the narrower subsonic regions on the minor axis plane for the elliptic cases.

From the static temperature distribution in Fig. 8, one obvious observation is that the jet mixing is poorer for the elliptic cases, as the undiluted fuel jet has not been completely dispersed in a significantly longer downstream distance until reaching the downstream cavity. The poor mixing can be explained by the shorter jet penetration depth, which causes an insufficient macromixing between the jet and the crossflow in the elliptic combustor cases. For the round combustor cases, the mixing layer only extends slightly downstream of the jet porthole, and the jet is completely dispersed before the middle of the upstream cavity. It can be concluded that the current elliptic combustor does not fulfill the initial design goal of increasing the jet mixing. However, one important advantage of the elliptic combustor is that the shrinkage in the minor axis direction of the elliptic burner section acts as a physical throat, which anchors the shock train in the isolator and provides relatively steady crossflow conditions for the downstream combustion. Thus, the elliptic combustor is supposed to have better combustion stability, which has been confirmed by the relative steady static pressure profiles in Fig. 5 and the similar flame distributions as the crossflow Mach number Ma changes from 2.5 to 3.0. However, for the round combustor cases, as the crossflow Mach number Ma increases, the shock train slides considerably downstream, and the peak pressure in Fig. 5 drops from 2.0 to 1.3 bar. A strong shock train consisting of multiple shock waves is in favor of the downstream combustion through increasing the temperature (to usually above 1200 K), which can reduce the ignition delay by several orders of magnitude, as shown in Fig. 1c. At Ma = 2.5, the high-temperature gas above 2000 K not only fills the whole upstream cavity but also propagates upstream to surround the jet root, indicating that intense heat release occurs immediately after the jet issued from its porthole. However, at Ma = 3.0, the leading half-part of the upstream cavity has a relatively low temperature (less than 2000 K). This is because those initial chain reactions corresponding to the fuel pyrolysis are endothermic overall and the chemical timescale approximately equal to the ignition delay [21] increases by orders of magnitude at a relatively low temperature. From the results, the upstream cavity plays the important role of fuel

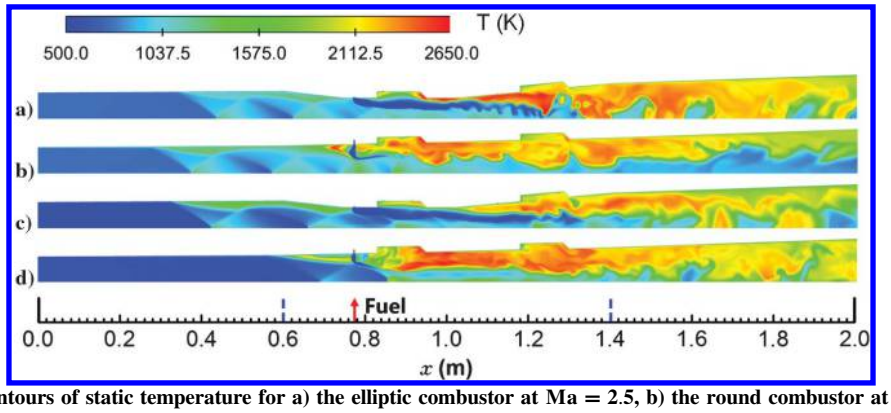

Fig. 8 Instantaneous contours of static temperature for a) the elliptic combustor at Ma = 2.5, b) the round combustor at Ma = 2.5, c) the elliptic combustor at Ma = 3.0, and d) the round combustor at Ma = 3.0.

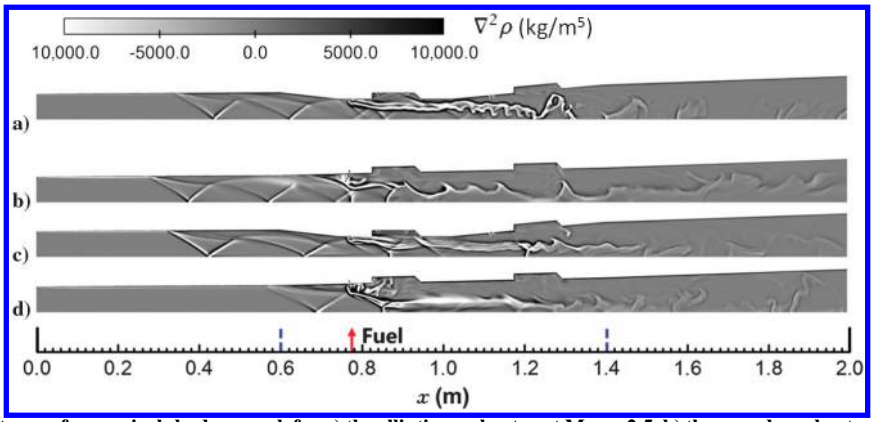

Fig. 9 Instantaneous contours of numerical shadowgraph for a) the elliptic combustor at Ma = 2.5, b) the round combustor at Ma = 2.5, c) the elliptic combustor at Ma = 3.0, and d) the round combustor at Ma = 3.0.

mixer and flame ignitor because high-temperature gas remains there all the way.

Figure 9 shows the instantaneous numerical shadowgraph represented by the Laplacian of the density field, which highlights the structures of the shock waves, high-density fuel stream, and hot-layer interfaces. The shock train consists of two shock waves, except for the round combustor case at Ma = 3.0, where most of the shock train has been swallowed into the burner and only one shock wave can be observed. At least two weaker shock waves reflected from the bow shock of the supersonic jet can be observed for the elliptic combustor cases. For the elliptic combustor cases, the penetration depth of the fuel stream is confirmed again to be lower, and the unburned fuel stream spreads further in the downstream than the round counterparts. The weaker shock waves intersect with the unburned fuel stream, which is helpful for the local fuel mixing through strengthening vortex generations [33]. The coherent plumelike interfaces in the expander are due to the interaction between the two-layer flow structures, i.e., the cold core flow and the high-temperature combustion gas attached to the wall.

The streamwise mixing and combustion efficiencies, as well as the total pressure loss for the two combustors under different crossflow Mach numbers Ma, are compared in Figs. 10 and 11. The mixing efficiency is calculated as

$$\eta_{\text{mix}} = \frac{\dot{m}_{\text{fuel,mixed}}}{\dot{m}_{\text{fuel,total}}} = \frac{\int Y_{f,\text{react}} \rho u \, \mathrm{d}A}{\int Y_f \rho u \, \mathrm{d}A} \tag{13}$$

with

$$Y_{f,\text{react}} = \begin{cases} Y_f & Y \le Y_{\text{st}} \\ Y_{f,\text{st}} \dfrac{1 - Y_f}{1 - Y_{f,\text{st}}} & Y > Y_{\text{st}} \end{cases}$$

where $\dot{m}_{\text{fuel,mixed}}$ and $\dot{m}_{\text{fuel,total}}$ are the mass flow rates of the mixed and total fuel, respectively; Y_f is the fuel mass fraction; $Y_{f,\text{react}}$ is the mass fraction of the fuel that can be reacted; and $Y_{f,\text{st}}$ is the fuel mass fraction at stoichiometric condition. The area integration is conducted on each cross section at a different streamwise location. The combustion efficiency is calculated as the ratio of the fuel that has been completely converted to the final stable products [e.g., carbon dioxide (CO_2) and water (H_2O)]. Due to the existence of H_2O in the incoming vitiated air, the definition of combustion efficiency based on H_2O for hydrogen combustion [34] is reformed to be based on CO_2 for hydrocarbon fuels:

$$\eta_c = \frac{\int_{\text{inlet}}^{x} (Y_{\text{CO}_2} \rho u) \, \mathrm{d}A / W_{\text{CO}_2}}{\dot{m}_{\text{fuel,total}} / W_{\text{fuel}}} \tag{14}$$

where the subscript "inlet" denotes variables on the inlet plane; the superscript x denotes the streamwise location; Y_{CO_2}, ρ, and u, are, respectively, the mass fraction of CO_2, the flow density, and the velocity; $\dot{m}_{\text{fuel}}$ is the mass flow rate of the fuel; and W is the molecular weight of the fuel or CO_2 denoted by the subscript. The total pressure loss is defined as [35]

$$\eta_{\text{t}} = 1 - \frac{\int (P_{t,x} \rho u) \, \mathrm{d}A}{\int (P_{t,\text{inlet}} \rho u) \, \mathrm{d}A} \tag{15}$$

where $P_{t,x}$ and $P_{t,\text{inlet}}$ are the total pressure at the streamwise location x and on the inlet plane, respectively.

From Fig. 10, it can be seen that the fuel mixing distance in the round combustor is much shorter than in the elliptic one, which is in accordance with the longer jet dispersion distances for the elliptic combustor cases shown in Fig. 7. Because the round combustor has a better near-field mixing, the initial combustion efficiency is higher than the elliptic combustor. However, the combustion efficiency in the elliptic combustor exceeds the round one after $x = 1.2$ m when sufficient fuel mixing has been accomplished. Combustion efficiencies at the combustor exit for the elliptic and round combustors are 76.7 and 59.7%, respectively, which both fail to meet the general threshold of 80% required for a scramjet engine to achieve net thrust. The total pressure losses have a small difference over the flowpath for the two combustors, finally reaching 71.1 and 64.4% at the combustor exit, respectively.

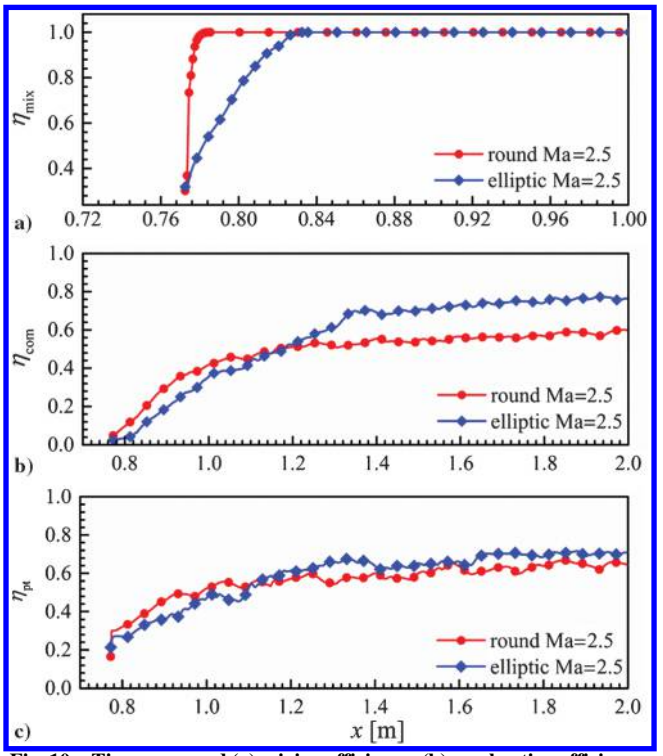

Fig. 10 Time-averaged (a) mixing efficiency, (b) combustion efficiency, and (c) total pressure loss for the elliptic and round combustors at Ma = 2.5.

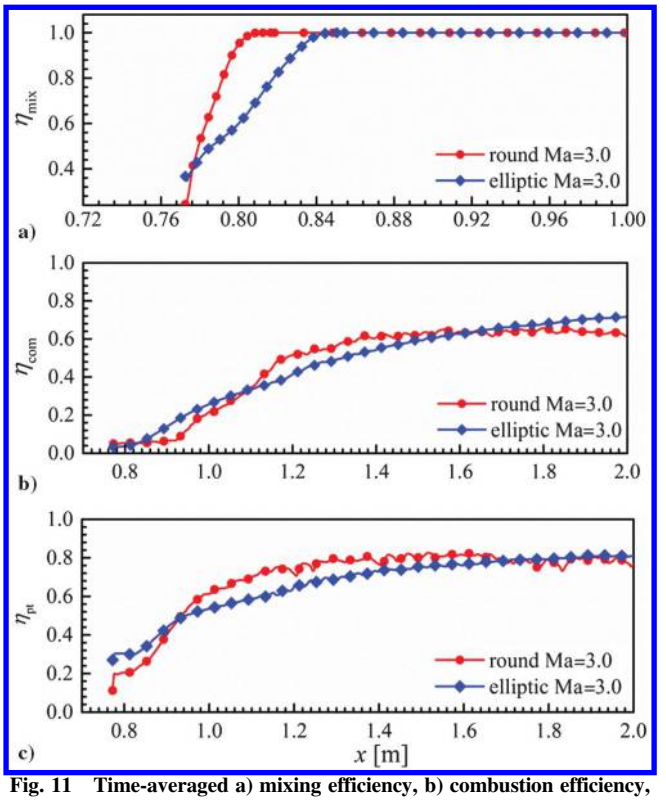

Fig. 11 Time-averaged a) mixing efficiency, b) combustion efficiency, and c) total pressure loss for the elliptic and round combustors at Ma = 3.0.

Because of the deeper penetration distance of the fuel jet in the round combustor, the greater momentum exchange causes a larger total pressure loss in the initial mixing stage before $x = 1.1$ m. However, the subsequently more violent heat release in the elliptical combustor aggravates its total pressure loss to beyond the round one by the Rayleigh heating loss effect. The sacrifice in a better near-field mixing is the usually a larger total pressure loss because more entropy is produced during the intense momentum exchange between the jet and the crossflow. Also, the excessive drag force caused by the varied cross-section shape of the elliptic burner section will generate more entropy and correspondingly larger total pressure loss.

From Fig. 11, the fuel mixing efficiencies deteriorate with the increasing of Mach number M for the two combustors, as indicated by the fully mixing distance. This can be explained by the decrease in the jet-to-crossflow momentum flux ratio as the crossflow Mach number Ma rises. As the Mach number Ma increases, the differences between the two combustors diminish for both the combustion efficiency and the total pressure loss. Under Ma = 3.0, the combustion efficiency decreases by 5.1 to 71.6% for the elliptic combustor; whereas it increases by 1.9 to 61.6% for the round one as compared with those under Ma = 2.5. The decrease in combustion efficiency for the round combustor is in accordance with Figs. 6 and 8, where the shock train slides downward considerably as the Mach number Ma increases, and the fuel jet is thereby exposed to a colder crossflow. As observed from Fig. 7, the fuel jet leans closer to the hot combustor wall without any active-cooling protection for Ma = 3.0, so the preheating by the wall and the boundary layer can be the reason for the increase in combustion efficiency for the elliptic combustor. Both the combustors suffer larger total pressure losses at higher Mach number Ma, i.e., 81 and 77%, respectively, for the elliptic and round combustors. The Rayleigh heating loss increases for the high inlet Mach number Ma, even when assuming roughly the same heat addition and friction effects. Actually, from the combustion efficiencies, the heat addition does increase for the elliptic combustor, whereas it varies little for the round one.

B. Wave Structures in the Elliptic Combustor

Due to the asymmetry of the elliptic cross section, the wave structures may appear as a unique spatial distribution. Figure 12 shows the three-dimensional wave structures in the elliptic combustor by the aid of intersected planes. Figure 12a shows that the oblique shock waves on the two planes, respectively, through the major and minor axes of the elliptic cross section are obviously similar in the axisymmetric isolator section. In the following burner section, the shock waves then deform differently in the two planes because the flow is expanding in the major axis direction but is compressed in the minor axis direction. The weak shock waves reflected from the bow shock wave are only observed on the minor axis plane because there is no jet injection on the major axis plane. However, due to the volume expansion of the hot combustion gas layer, one strong oblique shock wave and its weak reflection via the shear layer can be observed in the supersonic core flow. Figure 12b shows a close view of the main wave structures on the segment covering the isolator and burner sections. As seen, the waves in the shock train converge to one point on the axis, thus forming two pairs of funnel-shaped wave structures opposite each other in the three-dimensional tube. The shock train is then enveloped by a drum-shaped detached boundary layer in the neck region connecting the isolator and the burner. Figure 12c shows the Mach number Ma distribution delimited by the sonic line on the enlarged segment. Two cone low-Mach-number regions corresponding to the funnel-shaped waves can be clearly identified. The fuel jet is exposed to the low-Mach-number bay created after the second oblique shock wave in only a short distance because the Mach number Ma in the core flow then doubles quickly due to the shape expansion in the major axis direction. The supersonic region is continuous along the whole flowpath. The supersonic region gradually shrinks because of the upstream cavity and reaches the minimum near the downstream cavity; then, it expands again in the expander section. The current modeling results reveal that a vast and continuous subsonic region exists on the major axis plane, which is favorable for the mixing and combustion. If there is an injection along the major axis direction, the penetration can be much deeper because the local crossflow

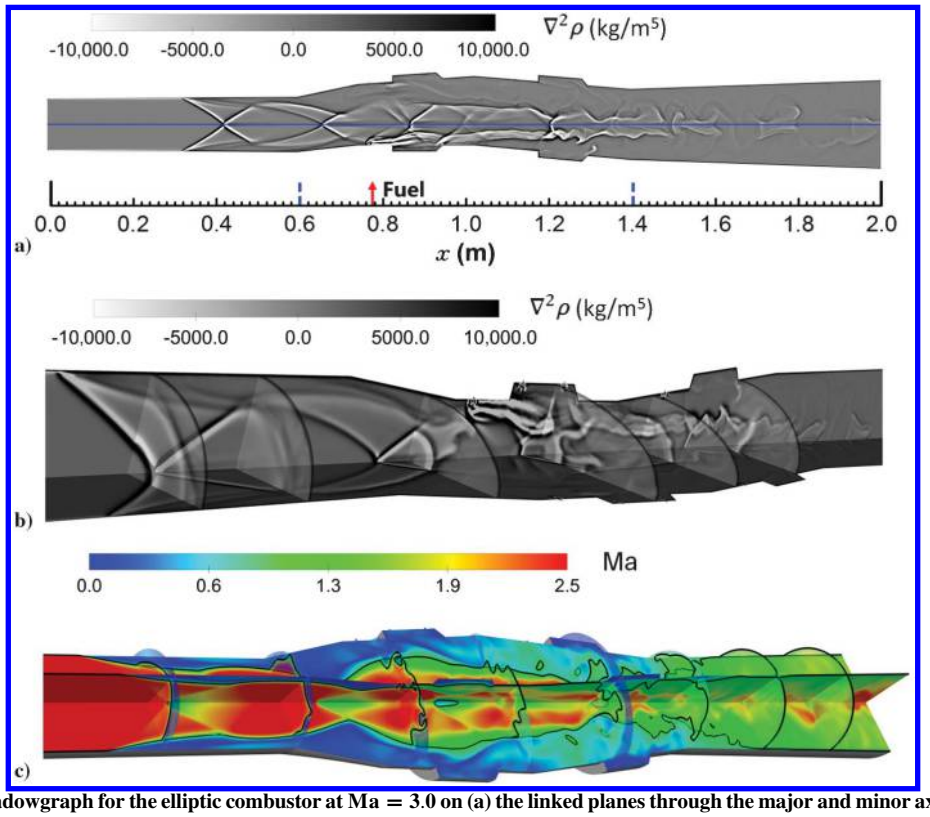

Fig. 12 Numerical shadowgraph for the elliptic combustor at Ma = 3.0 on (a) the linked planes through the major and minor axes, and (b) an enlarged segment covering the isolator and the burner; (c) three-dimensional Ma contour delimited by the black sonic line.

momentum flux (dynamic pressure) has been significantly reduced by the upstream shape transition. Therefore, in the future tests, injections along the major axis should be investigated. It is also interesting to note that the supersonic core region varies irregularly in shape from one streamwise location to another in the burner section due to the jet penetration and the heat addition.

C. Time Evolution of Wave and Flame Structures

Figure 13 shows the time average and the time evolution of the Mach number Ma contours over a certain quasi-steady period. From the mean Mach number Ma distribution, the subsonic region mainly distributes inside the convex part of the burner section, whereas the Mach number Ma in the supersonic core decreases to the minimum near the downstream cavity and then increases in the expander section again. The flow Mach number Ma is extremely low inside the two cavities and the backward-facing step (backstep) region immediately following the round-to-ellipse transition point. Those low-Mach-number bays should be favorable for the flame anchoring because the flow residence time is longer and large-scale vortices are produced in a similar manner to in the backstep problem. In the instantaneous fields, the subsonic region shrinks or expands considerably with a wavelike sonic interface. However, the initial position of the shock remains quite stable around the anchoring point, which is slightly before the shape-transition point. Actually, the shock train slides only slightly even under different crossflow Mach numbers Ma, as shown in Fig. 9. This is possible because the shrinkage in the minor axis direction when transitioning from round to elliptic cross sections acts as a converging throat, which raises the backpressure by compressing the supersonic flow, and hence anchors the upstream shock train. The flow then seems to accelerate intermittently in the expander, exhibiting as a discontinuous distribution of high-Mach-number regions. This indicates that large-scale coherent structures exist there and the turbulent flow is far from isotropic, even when approaching the combustor exit.

Figure 14 shows the time average and the time evolution of flame structures corresponding to the times in Fig. 13. Although the flame structure transforms its shape all the time, the time-averaged temperature field shows that two steady flame stabilization regions are the shear layer extending from the transition point and the mixing layer around the downstream cavity. The shape transitions from round to ellipse at the upstream and from ellipse to round at the downstream, respectively, from backstep- and frontstep-type flows, which can entrain oxygen from the crossflow through creating large-scale streamwise vortices. The oxygen enrichment and the low Mach number Ma are possibly the two main reasons for the flame stabilization there. Referring to Fig. 13, the flame regions mostly overlap with the subsonic regions but, still, a certain amount of combustion occurs under the supersonic condition. From the instantaneous fields, the flame resides along the shear/mixing layer because of the first shape-transition point, and then violent combustion occurs when approaching the next shape-transition point. The convex elliptic section seems to play the role of a large open cavity, which similarly provides a low-Mach-number bay and induces vortices to entrain air from the adjacent supersonic flow. Much weaker combustion occurs in the bottom of the "cavity," possibly because the convex depth limits the transport of enough oxygen to there. The striplike unburned fuel stream shown in Fig. 8 sometimes penetrates laterally and is observed as small low-temperature spots in Figs. 14c–14f. The core crossflow in low temperatures is gradually eroded by the expanding hot combustion layer in the burner section. The hot upper layer is entrained with the core flow, forming intermittent large-scale plume structures as the flow approaches the combustor exit.

A POD analysis [36] is conducted for the time evolution of temperature fields over the quasi-steady period to reveal the dominant patterns of coherent flame structures. Three hundred and eighty-three snapshots of the temperature field with a time interval of 20 μs are used to construct the least-order expansion of the snapshots:

$$T = \sum_{i=1}^{I} a_i(t) T_{\mathrm{POD},i} \tag{16}$$

where the time coefficient $a_i(t)$ is computed as the inner product (projection) between the snapshot and the spatial mode $T_{\mathrm{POD},i}$, and $T_{\mathrm{POD},i}$ is linearly combining the snapshots using the eigenvectors of the autocovariance of the snapshot matrix. Here, the eigenvectors are arranged in decreasing order of the corresponding eigenvalues as $\lambda_1 \geq \lambda_2 \geq, \ldots, \geq \lambda_I$. The POD eigenvalue spectrum calculated as $\lambda_i / \sum \lambda_i$ represents the relative amount of the total energy captured by the current POD mode. Figure 15 shows the relative energy percentage of the first 36 POD modes, where the first four modes have relatively higher energy, and are thus shown in Fig. 16. Mode 1 and mode 2 are visually similar for the high-temperature striplike region along the shear/mixing layer, which confirms the observation in Fig. 14 that the main combustion reactions occur along the interface between the cold

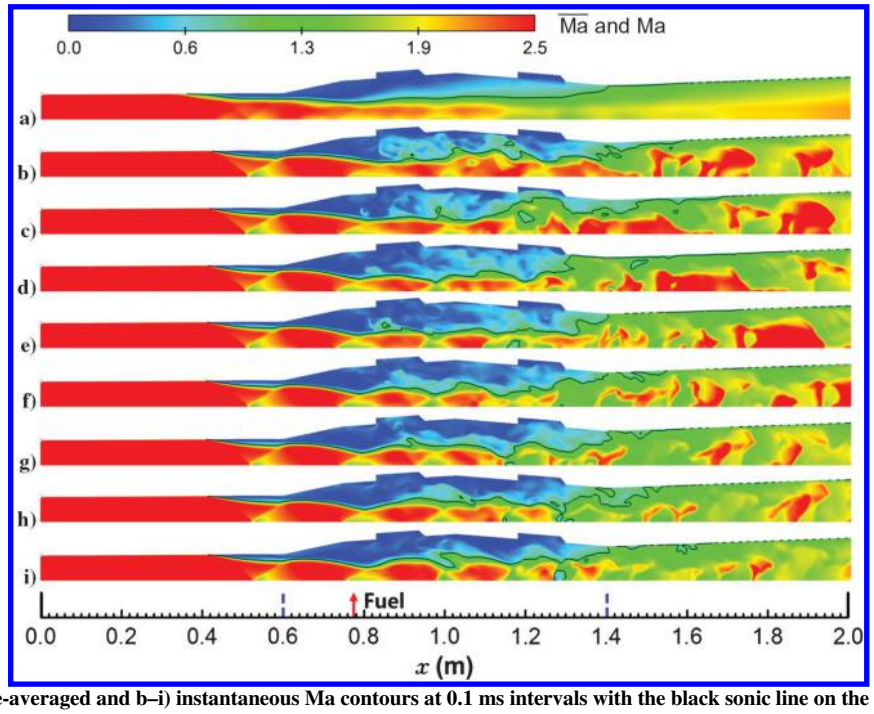

Fig. 13 a) Time-averaged and b–i) instantaneous Ma contours at 0.1 ms intervals with the black sonic line on the major axis plane.

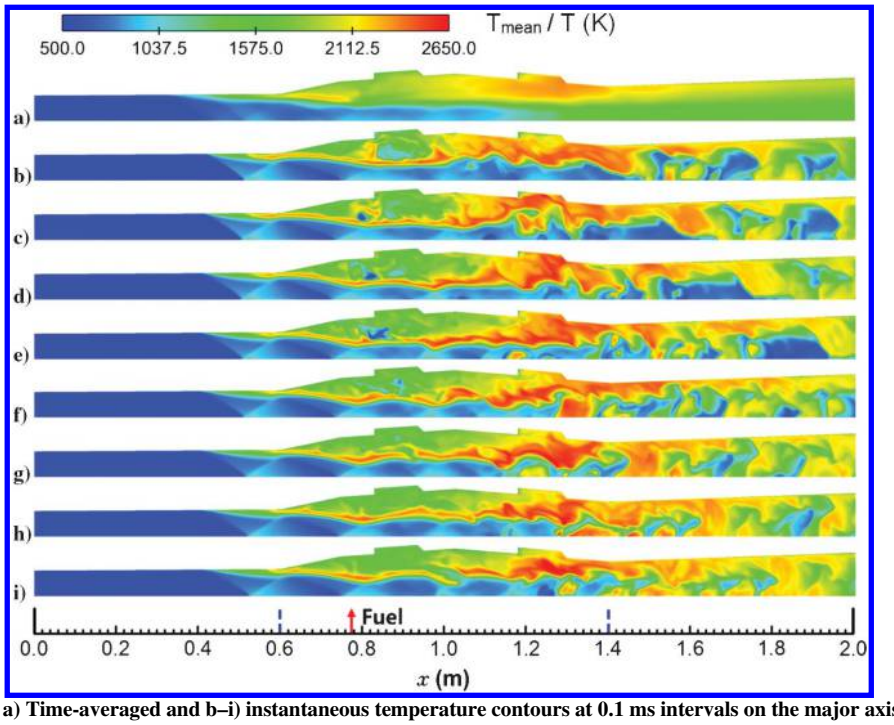

Fig. 14 a) Time-averaged and b–i) instantaneous temperature contours at 0.1 ms intervals on the major axis plane.

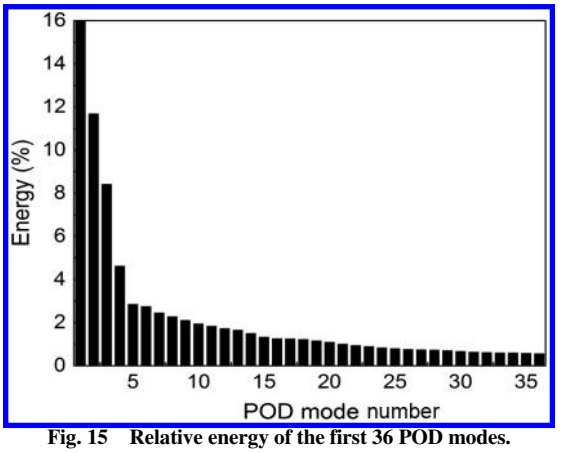

Fig. 15 Relative energy of the first 36 POD modes.

core flow and the hot near-wall layer. In mode 1, the postshock regions also have relatively high temperatures. Also shown in mode 1 is a thin hot layer attached to the wall, whereas another high-temperature striplike region distributes along the core flow in the expander, suggesting a distinct stratification phenomenon there. Mode 3 and mode 4 show discontinuous flame regions in the front part of the burner section and confirm the large attached flame region around the downstream cavity. The discontinuity indicates that the flame along the shear/mixing layer is intermittent during the time evolution. Mode 4 shows a longer attached flame region, even to the upstream cavity, implying that, during certain period of time, the flame also propagates upstream to there. Stratified high-temperature regions are also shown for the upper layer and the beneath-core flow, respectively, in modes 3 and 4. From the four modes, the flame in the expander exhibits a clear oscillation pattern, which corresponds to a collection of vortices due to the entrainment of the two stratified layers. Moreover, the layer closely attached to the expander shell always has a high temperature above 1300 K, implying that an additional cooling facility should be applied to protect it from melting if long-time operations are required.

IV. Conclusions

To explore the combustion performance of nonrectangular-type supersonic combustors, the flow and combustion characteristics of round and round-to-elliptic shape-transition supersonic combustors were compared, based on the measurements and the improved delayed detached-eddy simulation modeling results. Four cases with the same global fuel equivalence ratio of 0.8 but different inlet Mach numbers Ma of 2.5 and 3.0 were compared for both of the combustors. The modelings were based on a newly developed 19 s/54 r skeletal kerosene mechanism, which was even simpler than the previously used 28-species mechanism but agreed even better with the original 2185-species detailed mechanism in the key

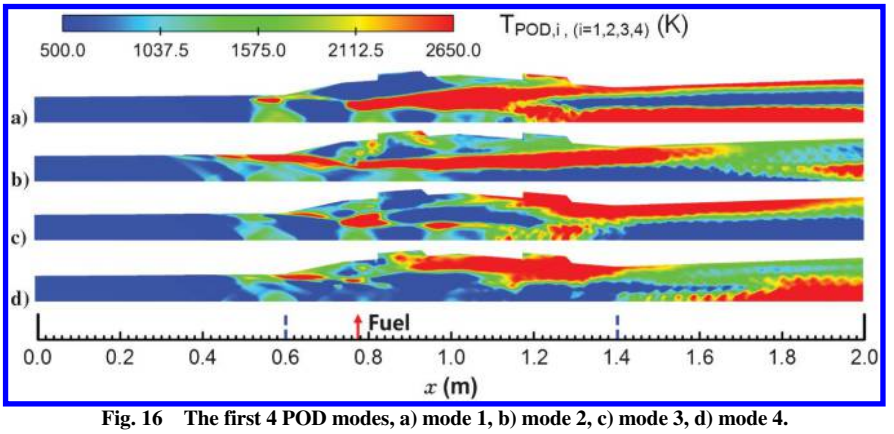

Fig. 16 The first 4 POD modes, a) mode 1, b) mode 2, c) mode 3, d) mode 4.

kinetic properties. A grid sensitivity analysis was conducted to assess the influence of global and local mesh resolutions on the pressure predictions.

The predicted and measured time-averaged static pressure in the streamwise direction agree reasonably for the two key aspects (i.e., the pressure rise ratio and the initial pressure rise location), indicating that the flame anchoring location and the distribution of wave structures inside the combustor are close to the real situation. The initial location of the shock train is insensitive to the inlet Mach number Ma for the elliptic combustor, but it slides downstream considerably and the peak pressure drops almost by half for the round combustor as the Mach number Ma rises from 2.5 to 3.0. The near-field mixing performance is better for the round combustor, but the final combustion efficiency is higher for the elliptic combustor. As the Mach number Ma increases, the mixing distances of the both combustors extend; the combustion efficiency increases for the elliptic combustor but drops slightly for the round one. The total pressure losses are close for the two combustors, and both increase considerably as the Mach number Ma increases.

The oblique shock waves on the planes through the major and minor axes of the elliptic cross section are obviously similar in the axisymmetric isolator section, but the shock waves deform differently on the two planes because the flow is expanding in the major axis direction but compressed in the minor axis direction. The shock train waves converge to one point on the combustor axis and form two pairs of funnel-shaped wave structures opposite to each other. The supersonic region is continuous along the whole flowpath and shrinks to the minimum near the downstream cavity.

The initial position of shock train remains quite stable from time to time and even under different crossflow Mach numbers Ma, suggesting that the shrinkage in the minor axis direction when transitioning from round to elliptic cross sections anchors the shock train. The shape transitions from round to ellipse, and then to round again, to form backstep- and frontstep-type flows, which stabilize the flame by providing a low-Mach-number bay and inducing vortices to entrain air from the adjacent supersonic flow; thus, the convex elliptic section actually plays the role of a large open cavity. Such anchoring effects in the shock train and the flame explain the better combustion stability of the elliptic combustor. A proper orthogonal decomposition analysis confirms the main combustion reactions along the mixing interface, discontinuous flame regions in the front part of the burner section, and the distinct stratification phenomenon in the expander.

Appendix: Skeletal Mechanism of Kerosene/O_2

Table A1 List of the reactions involved in the skeletal mechanism of kerosene/O_2 combustion (19 species and 54 steps) and coefficients for the calculation of rate constants[a]

No.	Reaction	A	n	E
1	$NC_{10}H_{22} \rightarrow 2C_3H_6 + 2CH_3 + C_2H_4$	$1.000 \cdot 10^{13}$	0.00	21,000.0
2	$IC_8H_{18} \rightarrow 2C_3H_6 + 2CH_3$	$1.000 \cdot 10^{13}$	0.00	21,000.0
3	$PCH \rightarrow 3C_2H_4 + C_3H_6$	$1.000 \cdot 10^{13}$	0.00	21,000.0
4	$H + H + M \rightleftharpoons H_2 + M$	$1.000 \cdot 10^{18}$	−1.0	0.0
	Third-body efficiencies: $H_2O = 16.25$; $CO = 1.875$; $CO_2 = 3.75$; $H_2 = 2.50$			
5	$H + O_2 \rightleftharpoons OH + O$	$1.900 \cdot 10^{14}$	0.0	16,812.0
6	$H + O_2 + M \rightleftharpoons HO_2 + M$	$8.000 \cdot 10^{17}$	−0.80	0.0
	Third-body efficiencies: $H_2O = 16.25$; $CO = 1.875$; $CO_2 = 3.75$; $H_2 = 2.50$			
7	$H + OH + M \rightleftharpoons H_2O + M$	$3.000 \cdot 10^{22}$	−2.0	0.0
	Third-body efficiencies: $H_2O = 16.25$; $CO = 1.875$;$CO_2 = 3.75$; $H_2 = 2.50$			
8	$H_2 + O_2 \rightleftharpoons OH + OH$	$1.700 \cdot 10^{13}$	0.0	47,780.0
9	$O + H_2 \rightleftharpoons OH + H$	$1.30 \cdot 10^{04}$	2.80	5,922.0
10	$H_2 + OH \rightleftharpoons H_2O + H$	$2.160 \cdot 10^{08}$	1.5	3,430.0
11	$O + O + M \rightleftharpoons O_2 + M$	$1.140 \cdot 10^{17}$	−1.0	0.0
	Third-body efficiencies: $H_2O = 16.25$; $CO = 1.875$; $CO_2 = 3.75$; $H_2 = 2.50$			
12	$O + H + M \rightleftharpoons OH + M$	$6.200 \cdot 10^{16}$	−0.6	0.0
	Third-body efficiencies: $H_2O = 16.25$; $CO = 1.875$; $CO_2 = 3.75$; $H_2 = 2.50$			
13	$H_2O + O \rightleftharpoons OH + OH$	$1.500 \cdot 10^{10}$	1.14	17,260.0
14	$HO_2 + OH \rightleftharpoons H_2O + O_2$	$1.450 \cdot 10^{13}$	0.0	−497.0
15	$HO_2 + O \rightleftharpoons OH + O_2$	$2.440 \cdot 10^{13}$	0.0	−446.0
16	$H + HO_2 \rightleftharpoons H_2 + O_2$	$2.140 \cdot 10^{13}$	0.0	1,411.0
17	$H + HO_2 \rightleftharpoons OH + OH$	$8.400 \cdot 10^{13}$	0.0	875.0
18	$H + HO_2 \rightleftharpoons H_2O + O$	$3.010 \cdot 10^{13}$	0.0	1,721.0
19	$CO + HO_2 \rightleftharpoons CO_2 + OH$	$1.150 \cdot 10^{05}$	2.30	17,550.0
20	$CO + OH \rightleftharpoons CO_2 + H$	$4.400 \cdot 10^{06}$	1.50	−740.0
21	$CO + O + M \rightleftharpoons CO_2 + M$	$2.830 \cdot 10^{13}$	0.0	−4, 540.0
	Third-body efficiencies: $H_2O = 16.25$; $CO = 1.875$; $CO_2 = 3.75$; $H_2 = 2.50$			
22	$CO + O_2 \rightleftharpoons CO_2 + O$	$2.530 \cdot 10^{12}$	0.0	47,700.0
23	$HCO + M \rightleftharpoons H + CO + M$	$2.300 \cdot 10^{17}$	−1.0	17,090.0
	Third-body efficiencies: $H_2O = 16.25$; $CO = 1.875$; $CO_2 = 3.75$; $H_2 = 2.50$			
24	$HCO + OH \rightleftharpoons CO + H_2O$	$1.000 \cdot 10^{14}$	0.0	0.0
25	$HCO + O \rightleftharpoons CO + OH$	$3.000 \cdot 10^{13}$	0.0	0.0
26	$HCO + O \rightleftharpoons CO_2 + H$	$3.000 \cdot 10^{13}$	0.0	0.0
27	$HCO + H \rightleftharpoons CO + H_2$	$7.220 \cdot 10^{13}$	0.0	0.0
28	$HCO + O_2 \rightleftharpoons CO + HO_2$	$7.580 \cdot 10^{12}$	0.0	410.0
29	$HCO + HO_2 \rightleftharpoons CO_2 + OH + H$	$3.000 \cdot 10^{13}$	0.0	0.0
30	$HCO + HCO \rightleftharpoons CH_2O + CO$	$1.200 \cdot 10^{13}$	0.0	0.0
31	$HCO + HCO \rightleftharpoons H_2 + CO + CO$	$3.000 \cdot 10^{12}$	0.0	0.0
32	$CH_3 + OH \rightleftharpoons CH_2O + H_2$	$7.390 \cdot 10^{14}$	−1.13	14,551.0
33	$CH_3 + O \rightleftharpoons H + CH_2O$	$8.430 \cdot 10^{13}$	0.0	0.0
34	$CH_3 + O \rightarrow H + H_2 + CO$	$3.370 \cdot 10^{13}$	0.0	0.0
35	$CH_3 + O2 \rightleftharpoons CH_2O + OH$	$6.620 \cdot 10^{11}$	0.00	14,188.0
36	$CH_2O + OH \rightleftharpoons HCO + H_2O$	$1.716 \cdot 10^{09}$	1.18	−447.0
37	$CH_2O + M \rightleftharpoons HCO + H + M$	$5.850 \cdot 10^{14}$	0.00	64,200.0

Table A1 (*Continued.*)

No.	Reaction	A	n	E
	Third-body efficiencies: $H_2O = 16.25$; $CO = 1.875$; $CO_2 = 3.75$; $H_2 = 2.50$			
38	$CH_2O + O \rightleftharpoons HCO + OH$	$1.810 \cdot 10^{13}$	0.00	3,088.0
39	$CH_2O + H \rightleftharpoons HCO + H_2$	$1.100 \cdot 10^{08}$	1.80	3,000.0
40	$CH_2O + O_2 \rightleftharpoons HCO + HO_2$	$1.230 \cdot 10^{06}$	3.00	52,000.0
41	$C_2H_4 + H_2 \rightleftharpoons CH_3 + CH_3$	$3.767 \cdot 10^{12}$	0.83	84,710.0
—	Reverse efficiencies	$1.000 \cdot 10^{14}$	0.00	32,000.0
42	$C_2H_4 + M \rightleftharpoons C_2H_3 + H + M$	$2.970 \cdot 10^{17}$	0.00	96,560.0
	Third-body efficiencies: $H_2O = 16.25$; $CO = 1.875$; $CO_2 = 3.75$			
43	$C_2H_4 + OH \rightleftharpoons C_2H_3 + H_2O$	$2.024 \cdot 10^{13}$	0.00	5,936.0
44	$C_2H_4 + O \rightleftharpoons CH_3 + HCO$	$1.200 \cdot 10^{08}$	1.44	530.0
45	$C_2H_4 + H \rightleftharpoons C_2H_3 + H_2$	$1.000 \cdot 10^{14}$	0.00	15,009.0
46	$C_2H_4 + O_2 \rightleftharpoons C_2H_3 + HO_2$	$4.220 \cdot 10^{13}$	0.00	57,629.0
47	$C_2H_3 + O_2 \rightleftharpoons CH_2O + HCO$	$9.275 \cdot 10^{25}$	−3.96	7,043.0
48	$C_2H_3 + HO_2 \rightarrow CH_3 + CO + OH$	$3.000 \cdot 10^{13}$	0.00	0.0
49	$C_2H_3 + O \rightleftharpoons CH_3 + CO$	$1.500 \cdot 10^{13}$	0.00	0.0
50	$C_2H_3 + HCO \rightleftharpoons C_2H_4 + CO$	$9.034 \cdot 10^{13}$	0.00	0.0
51	$C_2H_3 + CH_2O \rightleftharpoons C_2H_4 + HCO$	$5.420 \cdot 10^{03}$	2.81	5,862.0
52	$C_3H_6 \rightleftharpoons C_2H_3 + CH_3$	$1.100 \cdot 10^{21}$	−1.20	97,720.0
53	$C_3H_6 + O \rightleftharpoons C_2H_4 + CH_2O$	$7.020 \cdot 10^{07}$	1.57	−628.0
54	$C_3H_6 + H \rightleftharpoons C_2H_4 + CH_3$	$7.230 \cdot 10^{12}$	0.00	1,302.0

[a]Note that 1) the rate constant is given by the Arrhenius formula $k = AT^b \exp(-E/RT)$; 2) when third-body reactions are involved, the rate constant is multiplied by the third-body concentration given as $[C_M] = \sum_{\alpha=1}^{L} \gamma_\alpha [C_\alpha]$ with γ_α as the third-body coefficient for species α; and 3) the units for A and E are centimeters, mole, seconds, Kelvin, and cal/mole, respectively.

Acknowledgments

This project was supported by training program of the Major Research Plan of the National Natural Science Foundation of China (grant no. 91641110) and the National Natural Science Foundation of China (grant no. 11502270). The authors are also grateful to National Supercomputing Center of Tianjin for providing computational resources.

References

[1] Doherty, L. J., Smart, M. K., and Mee, D. J., "Experimental Testing of an Airframe-Integrated Three-Dimensional Scramjet at Mach 10," *AIAA Journal*, Vol. 53, No. 11, 2015, pp. 3196–3207. doi:10.2514/1.J053785

[2] Suraweera, M. V., and Smart, M. K., "Shock-Tunnel Experiments with a Mach 12 Rectangular-to-Elliptical Shape-Transition Scramjet at Offdesign Conditions," *Journal of Propulsion and Power*, Vol. 25, No. 3, 2009, pp. 555–564. doi:10.2514/1.37946

[3] Smart, M. K., "Experimental Testing of a Hypersonic Inlet with Rectangular-to-Elliptical Shape Transition," *Journal of Propulsion and Power*, Vol. 17, No. 2, 2001, pp. 276–283. doi:10.2514/2.5774

[4] Gollan, R., and Ferlemann, P., "Investigation of Rest-Class Hypersonic Inlet Designs," AIAA Paper 2011-2254, 2011. doi:10.2514/6.2011-2254

[5] Hartill, W. B., "Analytical and Experimental Investigation of a Scramjet Inlet of Quadriform Shape," U.S. Air Force Rept. AFAPL-TR-65-74, 1965.

[6] Gruber, M., Smith, S., and Mathur, T., "Experimental Characterization of Hydrocarbon-Fueled, Axisymmetric, Scramjet Combustor Flowpaths," AIAA Paper 2011-2311, 2011. doi:10.2514/6.2011-2311

[7] Smith, S., Gruber, M., Steiner, R., Collatz, M., and Mathur, T., "Development and Calibration of an Axisymmetric Direct-Connect Supersonic-Combustion Flowpath," AIAA Paper 2009-5035, 2009. doi:10.2514/6.2009-5035

[8] David, P., Russell, B., and Vincent, W., "Hybrid Reynolds-Averaged and Large-Eddy Simulation of Mixing in an Axisymmetric Scramjet," AIAA Paper 2012-5902, 2012. doi:10.2514/6.2012-5902

[9] Houshang, E., Datta, G., and Faure, M.-M., "Exploratory RANS and LES Simulations of Transient Supersonic Combustor Flow," AIAA Paper 2009-0128, 2009. doi:10.2514/6.2009-128

[10] Skare, P. E., and Krogstad, P.-A., "A Turbulent Equilibrium Boundary Layer near Separation," *Journal of Fluid Mechanics*, Vol. 272, Aug. 1994, pp. 319–348. doi:10.1017/S0022112094004489

[11] Kee, R. J., Rupley, F. M., and Miller, J. A., "Chemkin-II: A Fortran Chemical Kinetics Package for the Analysis of Gas-Phase Chemical Kinetics," Sandia National Labs. TR SAND89-8009B, Albuquerque, NM, 1989.

[12] Chase, M. W., "NIST-JANAF Thermochemical Tables 2 Volume-Set," *Journal of Physical and Chemical Reference Data Monograph*, Vol. 9, Aug. 1998.

[13] Bird, R. B., Stewart, W. E., and Lightfoot, E. N., *Transport Phenomena*, 2nd ed., Wiley, New York, 2002, p. 84.

[14] Mathur, S., Tondon, P. K., and Saxena, S. C., "Thermal Conductivity of Binary, Ternary and Quaternary Mixtures of Rare Gases," *Molecular Physics*, Vol. 12, No. 6, 1967, pp. 569–579. doi:10.1080/00268976700100731

[15] Spalart, P. R., Jou, W. H., Strelets, M., and Allmaras, S. R., "Comments on the Feasibility of LES for Wings and a Hybrid RANS/LES Approach," *Proceedings of the First AFOSR Conference on DNS/LES*, Greyden Press, Columbus, Aug. 1997, pp. 137–147.

[16] Travin, A. K., Shur, M. L., Spalart, P. R., and Strelets, M. K., "Improvement of Delayed Detached-Eddy Simulation for LES with Wall Modelling," *Part of: ECCOMAS CFD 2006: Proceedings of the European Conference on Computational Fluid Dynamics*, Delft Univ. of Technology, Delft, The Netherlands, Sept. 2006.

[17] Spalart, P. R., and Allmaras, S. R., "A One-Equation Turbulence Model for Aerodynamic Flows," AIAA Paper 1992-0439, 1992. doi:10.2514/6.1992-439

[18] Dagaut, P., Karsenty, F., Dayma, G., Diévart, P., Hadj-Ali, K., Mzé-Ahmed, A., Braun-Unkhoff, M., Herzler, J., Kathrotia, T., Kick, T., Naumann, C., Riedel, U., and Thomas, L., "Experimental and Detailed Kinetic Model for the Oxidation of a Gas to Liquid (GtL) Jet Fuel," *Combustion and Flame*, Vol. 161, No. 3, 2014, pp. 835–847. doi:10.1016/j.combustflame.2013.08.015

[19] Yao, W., Wang, J., Lu, Y., and Fan, X., "Skeletal Mechanism Generation Based on DRGEPSA for Daqing RP-3 Aviation Kerosene and Numerical Validation," *7th National Conference on Hypersonic Science and Technology*, Hypersonic Reseach Center CAS, CSTAM2014-A62-B0044, Beijing, Oct. 2014.

[20] Yao, W., Wang, J., Lu, Y., Li, X., and Fan, X., "Full-Scale Detached Eddy Simulation of Kerosene Fueled Scramjet Combustor Based on Skeletal Mechanism," AIAA Paper 2015-3579, 2015. doi:10.2514/6.2015-3579

[21] Yao, W., Lu, Y., Li, X., Wang, J., and Fan, X., "Improved Delayed Detached Eddy Simulation of a High-Ma Active-Cooled Scramjet Combustor Based on Skeletal Kerosene Mechanism," AIAA Paper 2016-4761, 2016. doi:10.2514/6.2016-4761

[22] Niemeyer, K. E., Sung, C.-J., and Raju, M. P., "Skeletal Mechanism Generation for Surrogate Fuels Using Directed Relation Graph with Error Propagation and Sensitivity Analysis," *Combustion and Flame*, Vol. 157, No. 9, 2010, pp. 1760–1770. doi:10.1016/j.combustflame.2009.12.022

[23] Golovitchev, V. I., Nordin, N., Jarnicki, R., and Chomiak, J., "3-D Diesel Spray Simulations Using a New Detailed Chemistry Turbulent Combustion Model," SAE Technical Paper 2000-01-1891, Warrendale, PA, 2000. doi:10.4271/2000-01-1891

[24] Pope, S. B., "Computationally Efficient Implementation of Combustion Chemistry Using in Situ Adaptive Tabulation," *Combustion Theory and Modeling*, Vol. 1, No. 1, 1997, pp. 41–63. doi:10.1080/713665229

[25] Kusaka, J., Horie, N., Daisho, Y., and Nakayama, S., "Numerical Simulation Accounting for the Finite-Rate Elementary Chemical Reactions for Computing Diesel Combustion Process," *SAE Technical Papers*, Vol. 2005, Capril, Napoli, Sept. 2005. doi:10.4271/2005-24-051

[26] Greenshields, C. J., Weller, H. G., Gasparini, L., and Reese, J. M., "Implementation of Semi-Discrete, Non-Staggered Central Schemes in a Colocated, Polyhedral, Finite Volume Framework, for High-Speed Viscous Flows," *International Journal for Numerical Methods in Fluids*, Vol. 38, No. 2, 2009, pp. 139–161. doi:10.1002/fld.2069

[27] Wu, K., Li, X., Yao, W., and Fan, X., "Three-Dimensional Numerical Study of the Acoustic Properties of a Highly Underexpanded Jet," AIAA Paper 2015-3572, 2015. doi:10.2514/6.2015-3572

[28] Li, X., Wu, K., Yao, W., and Fan, X., "A Comparative Study of Highly Underexpanded Nitrogen and Hydrogen Jets Using Large Eddy Simulation," AIAA Paper 2015-3573, 2015. doi:10.2514/6.2015-3573

[29] Li, X., Yao, W., and Fan, X., "Large-Eddy Simulation of Time Evolution and Instability of Highly Underexpanded Sonic Jets," *AIAA Journal*, Vol. 54, No. 10, 2016, pp. 3191–3211. doi:10.2514/1.J054689

[30] Liu, P., He, G., Hu, Z., and Zhang, M., "Large-Eddy Simulation of Kerosene Spray Combustion in a Model Scramjet Chamber," *Journal of Aerospace Engineering*, Vol. 224, No. 9, 2010, pp. 949–960. doi:10.1243/09544100jaero738

[31] Fureby, C., Chapuis, M., Fedina, E., and Karl, S., "CFD Analysis of the Hyshot II Scramjet Combustor," *Proceedings of the Combustion Institute*, Vol. 33, No. 2, 2011, pp. 2399–2405. doi:10.1016/j.proci.2010.07.055

[32] Gruber, M. R., Nejadt, A. S., Chen, T. H., and Dutton, J. C., "Mixing and Penetration Studies of Sonic Jets in a Mach 2 Freestream," *Journal of Propulsion and Power*, Vol. 11, No. 2, 1995, pp. 315–323. doi:10.2514/3.51427

[33] Génin, F., and Menon, S., "Studies of Shock/Turbulent Shear Layer Interaction Using Large-Eddy Simulation," *Computers and Fluids*, Vol. 39, No. 5, 2010, pp. 800–819. doi:10.1016/j.compfluid.2009.12.008

[34] Kumaran, K., and Babu, V., "Investigation of the Effect of Chemistry Models on the Numerical Predictions of the Supersonic Combustion of Hydrogen," *Combustion and Flame*, Vol. 156, No. 4, 2009, pp. 826–841. doi:10.1016/j.combustflame.2009.01.008

[35] Rajasekaran, A., and Babu, V., "Numerical Simulation of Three-Dimensional Reacting Flow in a Model Supersonic Combustor," *Journal of Propulsion and Power*, Vol. 22, No. 4, 2006, pp. 820–827. doi:10.2514/1.14952

[36] Berkooz, G., Holmes, P., and Lumley, J. L., "The Proper Orthogonal Decomposition in the Analysis of Turbulent Flows," *Annual Review of Fluid Mechanics*, Vol. 25, Jan. 1993, pp. 539–75. doi:10.1146/annurev.fl.25.010193.002543

J. C. Oefelein
Associate Editor